

Article

Porous Nb₂O₅ Nanofibers Prepared via Reactive Needle-Less Electrospinning for Application in Lithium–Sulfur Batteries

Ivan Shepa ^{1,*}, Erika Mudra ¹, Dominika Capkova ^{2,3}, Alexandra Kovalcikova ¹, Ondrej Petrus ¹, Frantisek Kromka ¹, Ondrej Milkovic ¹, Vitaliy Antal ⁴, Matej Balaz ⁵, Maksym Lisnichuk ^{1,6}, Dominika Marcin-Behunova ⁵, Dóra Zalka ^{1,6} and Jan Dusza ¹

- ¹ Institute of Materials Research, Slovak Academy of Sciences, Watsonova 47, 040 01 Kosice, Slovakia; emudra@saske.sk (E.M.); akovalcikova@saske.sk (A.K.); opetrus@saske.sk (O.P.); fkromka@saske.sk (F.K.); omilkovic@saske.sk (O.M.); maksym.lisnichuk@upjs.sk (M.L.); dzalka@saske.sk (D.Z.); jdusza@saske.sk (J.D.)
- ² Department of Physical Chemistry, Pavol Jozef Safarik University in Kosice, 041 54 Kosice, Slovakia; dominika.capkova@upjs.sk
- ³ Department of Chemical Sciences, Bernal Institute, University of Limerick, V94 T9PX Limerick, Ireland
- ⁴ Institute of Experimental Physics, Slovak Academy of Sciences, Watsonova 47, 040 01 Kosice, Slovakia
- ⁵ Institute of Geotechnics, Slovak Academy of Sciences, Watsonova 45, 040 01 Kosice, Slovakia; balazm@saske.sk (M.B.); behunova@saske.sk (D.M.-B.)
- ⁶ Department of Condensed Matter Physics, Institute of Physics, Faculty of Science, P.J. Šafárik University in Kosice, Park Angelinum 9, 041 54 Kosice, Slovakia
- * Correspondence: ishepa@saske.sk

Abstract: This contribution describes the preparation, coupled with detailed characterization, of Nb₂O₅ nanofibers and their application in lithium–sulfur batteries for the improvement of electrochemical performance. The utilization of reactive needle-less electrospinning allowed us to obtain, in a single step, amorphous pre-ceramic composite PAN/Nb₂O₅ fibers, which were transformed into porous ceramic Nb₂O₅ nanofibers via calcination. Thermogravimetric studies defined that calcination at 600 °C results in crystalline ceramic fibers without carbon residues. The fibrous morphology and mean diameter (614 ± 100 nm) of the ceramic nanofibers were analyzed via scanning and transmission electron microscopy. A surface area of 7.472 m²/g was determined through nitrogen adsorption measurements, while a combination of X-ray diffraction and Raman spectroscopy was used to show the crystallinity and composition of the fibers after calcination—single T-phase Nb₂O₅. Its performance in the cathode of lithium–sulfur batteries was defined through electrochemical tests, and the obtained results were compared to a similar blank electrode. The initial discharge capacity of 0.5 C reached a value of 570 mAh·g⁻¹, while the reversible capacity of 406 mAh·g⁻¹ was retained after 200 cycles, representing a capacity retention of 71.3%. The presence of Nb₂O₅ nanofibers in the carbon cathode inhibits the shuttle effect through polysulphide confinement, which originates from porosity and chemical trapping.

Keywords: niobia; nanofibers; needle-less electrospinning; oxide ceramics; lithium–sulfur batteries



Citation: Shepa, I.; Mudra, E.; Capkova, D.; Kovalcikova, A.; Petrus, O.; Kromka, F.; Milkovic, O.; Antal, V.; Balaz, M.; Lisnichuk, M.; et al. Porous Nb₂O₅ Nanofibers Prepared via Reactive Needle-Less Electrospinning for Application in Lithium–Sulfur Batteries. *Inorganics* **2023**, *11*, 456. <https://doi.org/10.3390/inorganics11120456>

Academic Editor: Christian Julien

Received: 27 October 2023

Revised: 15 November 2023

Accepted: 17 November 2023

Published: 25 November 2023



Copyright: © 2023 by the authors. Licensee MDPI, Basel, Switzerland. This article is an open access article distributed under the terms and conditions of the Creative Commons Attribution (CC BY) license (<https://creativecommons.org/licenses/by/4.0/>).

1. Introduction

The increasing demand for green and sustainable energy, driven by excessive fossil fuel consumption, environmental concerns, and the rise of electric vehicles, has highlighted the importance of rechargeable batteries. For years, batteries such as lead–acid, Ni–MH, Ni–Cd, and lithium-ion have dominated the electronic markets. Since their commercialization in the 1990s, lithium-ion batteries (LIBs) have become the preferred energy storage equipment for hybrid electric vehicles, electric vehicles, and electric tools due to their high energy density and long life cycle [1,2]. However, the energy density of traditional lithium-ion batteries is no longer sufficient to meet the rapidly growing needs of portable electronics. Along with issues with their short life cycle, recycling, and capacity, the wide

application of LIBs also raises some safety concerns regarding the utilization of flammable, toxic, and scarce materials [3,4]. As a result, researchers are now focused on exploring new electrode materials that can offer higher safety, energy, and power densities, along with lower costs and toxicity [1,3,5]. With more than three decades of development of rechargeable lithium-ion batteries (LIBs), a variety of electrode active materials was tested: oxide ceramics, carbon polymorphs, etc. Meanwhile, lithium–sulfur batteries (LSBs) are seen as the most promising successors to rechargeable LIBs due to their superior theoretical energy density of 2600 Wh kg^{-1} and theoretical capacity of $1675 \text{ mAh}\cdot\text{g}^{-1}$ [4,6,7]. Despite the low cost, low toxicity, and wide natural abundance of sulfur, LSBs have their drawbacks and face challenges such as the formation of polysulfides, the loss of active sulfur, its dissolution/diffusion in the electrolyte during the discharge cycle, the so-called shuttle effect, and the volume expansion of the cathode containing S. In LSBs, the shuttle effect is one of the main reasons for capacity decay and low charge efficiency [6–8]. Soluble long-chain polysulfides migrate to the lithium anode and react irreversibly, and then they form shorter polysulfides, which again flow back to the cathode. One of the accepted approaches to eliminate or at least minimize this shuttle effect is to introduce cathode materials, which have an affinity towards polysulfides and can adsorb or immobilize on their surfaces or catalytically convert soluble polysulfides into shorter ones already in the cathode; thus, they arrest the migration of polysulfides towards Li surfaces. The diffusion of polysulfides into the electrolyte will result in capacity decay, a lowering of the Coulombic efficiency, and the uncontrollable deposition of Li_2S_2 , Li_2S , and sulfur [6,7].

Metal oxides are the most promising inorganic compounds to anchor polysulfides in LSBs [8]. Especially in a nanostructured form, they have many advantages, among which are their high specific surface area and strong adsorption ability based on both physical and chemisorption [2,9]. A high surface area, along with often high conductivity, results in an increased contact area between the electrode and the electrolyte, which can inhibit the dissolution of the discharge products into the electrolyte, lower the internal resistance, and allow the cells to operate at higher current densities. Thanks to the oxidation state of O^{2-} metal oxides provide a strong polar surface, which efficiently traps hydrophilic lithium polysulfides and improves the utilization of elemental sulfur, while the covalent nature of the metal–oxygen bond guarantees high chemical stability and insolubility in most organic solvents [9]. Moreover, the volumetric energy density of LSBs can be enhanced by fabricating composite cathodes based on nanostructured metal oxides and sulfur, resulting in a cathode that is capable of trapping the discharge products inside or in the vicinity of the cathode, which can promote a conversion reaction between polysulfide intermediates and $\text{Li}_2\text{S}_2/\text{Li}_2\text{S}$ [4,9]. It was found that polar metal oxides can absorb sulfur species due to their intrinsic hydrophilic surfaces, and the surface acidity can sufficiently enhance the chemisorption ability of the metal oxides: the stronger the surface acidity of the metal oxide host, the higher the capability of polysulfide chemisorption [9–11]. Combining the high surface area with a chemical binding ability may heavily enhance the potential of metal oxide-based composite cathodes; this is why, recently, compounds of transition metals (especially of groups 4 and 5) have received great attention for their potential applications in renewable energy generation and storage; these include photocatalysis for water decontamination or splitting, electrodes in lithium–sulfur (LSBs), lithium (LIBs), sodium, and other ion batteries, and even supercapacitors [12–20]. Metal oxides, such as MnO_2 , Al_2O_3 , MgO , SiO_2 , Nb_2O_5 , and TiO_2 , as well as Magnéli phases like Ti_4O_7 , have been widely investigated due to their intense chemical binding energy with lithium polysulfides, which can suppress their irreversible dissolution within the electrolyte during the charge/discharge processes [1,6,8–10,21,22].

Niobium (V) oxide— Nb_2O_5 or also known as niobia, is a white, optically transparent (due to its large band gap), air-stable, water-insoluble solid [23,24]. It is one of the most important transition metal oxides. While niobia can be described as amphoteric, it is typically a chemically inert substance. Its structure is notably complex, temperature-dependent, and shows a wide range of polymorphism, necessitating a thorough combination of characteri-

zation techniques to determine the precise phase composition [17,18,23,25]. It is an n-type semiconductor with a bandgap, dependent on an oxygen stoichiometry, ranging between 3.2 to 4 eV. Stoichiometric Nb₂O₅ is an insulator with the conductivity of $\sigma \sim 3 \times 10^{-6} \text{ Scm}^{-1}$ and becomes semiconducting with a decrease in oxygen stoichiometry to Nb₂O_{4.8}, reaching the conductivity of $\sigma \sim 3 \times 10^{-3} \text{ Scm}^{-1}$ [18,26]. It is mainly used in the production of niobium metal; however, it has special applications in electronics, as the dielectric layer in capacitors in particular [27], thanks to its high dielectric constant. Also, it has a high refractive index, shows an electro-optic effect, and thus is often used in optoelectronics, optical glasses, photoelectrodes in dye-sensitized solar cells, and sensors [18,24,28]. Its unique properties paved the way for Nb₂O₅ in catalysis, where it is used for dehydration (of alcohols and esters), oxidation, reduction, hydrolysis, and polymerization [13,23,24,29,30].

Niobium oxide is considered a potential material for the negative electrodes in LIBs thanks to its rich redox chemistry (Nb⁵⁺ to Nb⁺), tunable acidity, chemical stability, and the presence of numerous stable and metastable polymorphs [9,10,17,18,25,26,31]. However, in the age of post-lithium batteries, such as lithium-sulfur LSBs, the application of Nb₂O₅ may help improve not only the overall performance of the battery but also solve some essential problems of limited lifetime and the so-called shuttle effect [1,9,10,21,26].

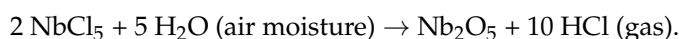
All bulk forms of Nb₂O₅ suffer poor electronic conductivity, along with sluggish Li⁺ diffusion [1,15,21]. To solve these issues, a large amount of efforts have been conducted recently. Generally, the fast charging/discharging performance of electrode materials is closely related to three key factors: kinetics of ion transport, electronic conductivity, and kinetics of interfacial and Faradaic reactions. In other words, the Li storage kinetics of Nb₂O₅ depend on charge and mass transfers near the reaction interfacial regions. Based on this concept, various optimizing strategies have been proposed. They can be summarized in the following two main directions [1,17,21,26]: (1) designing unique structures or morphologies, such as nanobelts, nanoplates, nanosheets, nanofibers, etc., to increase the specific surface area of the materials and shorten the path of charge transfer; (2) compositing with high conductive materials (such as metal NPs and carbon materials) [26].

This work is focused on the preparation and detailed characterization of the crystalline ceramic Nb₂O₅ nanofibers as a new potential additive in the cathode material for application in lithium-sulfur batteries.

2. Results and Discussion

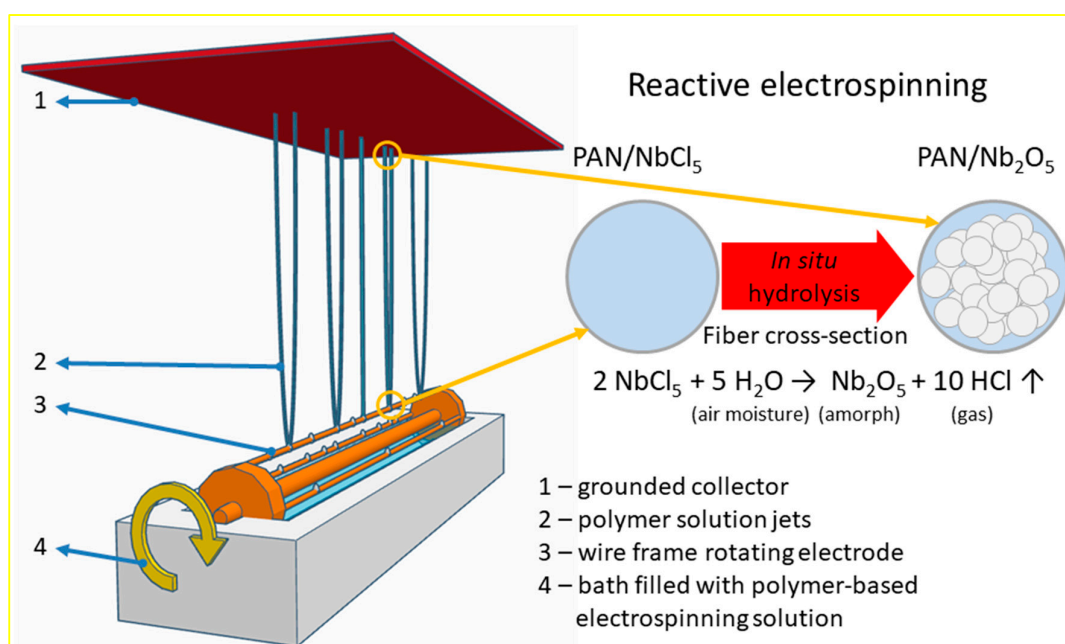
In this work, the preparation sequence of the ceramic Nb₂O₅ nanofibers can be divided into three basic steps:

- (I) The blending of the precursor solution containing the mandatory support polymer and the ceramic precursor.
- (II) Electrospinning itself. The precursor fibers were electrospun by the needleless reactive approach in which the ceramic component is synthesized in situ during the fibers formation and collection. Here, reactive electrospinning includes the initial transformation reaction of the ceramic precursor—hydrolysis of NbCl₅ by the air moisture to amorphous hydrated Nb₂O₅ trapped inside the PAN polymer fibers, thus resulting in amorphous pre-ceramic/polymer composite precursor fibers marked as PAN/Nb₂O₅:



Scheme 1 below describes the reactive nature of the electrospinning approach used in this work. The 3D model of the wire frame electrospinning electrode and a bath containing the polymer solution (part of the chamber of the Nanospider NSLab200) was modeled by Tinkercad 3D modeling software.

- (III) The last one is the preparation of the ceramic nanofibers by heat treatment of the composite precursor PAN/Nb₂O₅ fibers, resulting in the final crystalline Nb₂O₅ nanofibers (Nb₂O₅ NFs).



Scheme 1. Description of the reactive electrospinning approach used in this work.

2.1. Structural Characterization

Thermal analysis. DTA/TG analysis was carried out to explore the calcination process and define the phase transitions occurring in the precursor fibers. A small amount of the precursor fibers was put into a dedicated corundum crucible and calcined with a heating rate of 10 °C/min. The DTA/TG curves presented in Figure 1 show that there are three decomposition stages corresponding to the cyclization of PAN, decomposition–carbonization, and thermo-oxidation of carbon residues, separated by two exothermic peaks at 271 and 480 °C [32–34], corresponding to the gradual decomposition of PAN and crystallization of Nb₂O₅. The TG signals showed a mass loss accompanying the DTA signal in the temperature intervals from 40 °C to 271 °C and from 271 °C to approximately 590 °C [33,34]. The first mass loss event, in the vicinity of 50 °C, is caused by an onset of the evolution of physisorbed water and trapped HCl gas. Water is absorbed by the formed hydrated niobium pentoxide, which is formed by the hydrolysis of the niobium pentachloride with air moisture, resulting in the formation of the particles of amorphous Nb₂O₅ and HCl gas, which can be trapped inside the polymer and in porous amorphous ceramics. This hydrolysis takes place in situ during the electrospinning process at the moment of the fiber formation and is accelerated by the increased contact area of the ceramic precursor with the moisture in the air (see Scheme 1).

The first stage of the polymer degradation corresponds to the main crosslinking reaction, which is responsible for building up the polymeric network inside the fibers and usually emerges in the temperature range around 250–300 °C, but often depends on the purity of PAN; the treatment atmosphere (inert or oxidative) and presence of various other additives [32,35,36]. A lot of volatile by-products evolved during this stage [37], such as HCN and NH₃ [38].

The second stage in the literature ranged from about 320–360 °C to 440–480 °C and was defined to be a decomposition–carbonization process of cyclic structure with the volatilization of H₂ [36]. Here, the formed organic network begins to decompose in the temperature range from 271 °C to 590 °C, causing a partial weight loss of about 45.7%. A sharp exothermic peak appears at 480 °C at the end of this stage, which corresponds to the combustion of the organic and carbon residuals. The right shoulder of the peak, which causes its broadening, can be ascribed to the signal from the crystallization of Nb₂O₅ from the amorphous part of the precursor fibers. In this study, the third stage is short and

is presented in the temperature range of 590–610 °C, where the trace residues of carbon are oxidized and finally removed from the system. The total weight loss of the sample is detected to be up to 66.10%. As the temperature is raised over 600 °C, the weight of the products tends to be stable, and no further peaks are detected; this meant that all volatile or combustible residues had been fully removed from the sample, and only the ceramic component was presented.

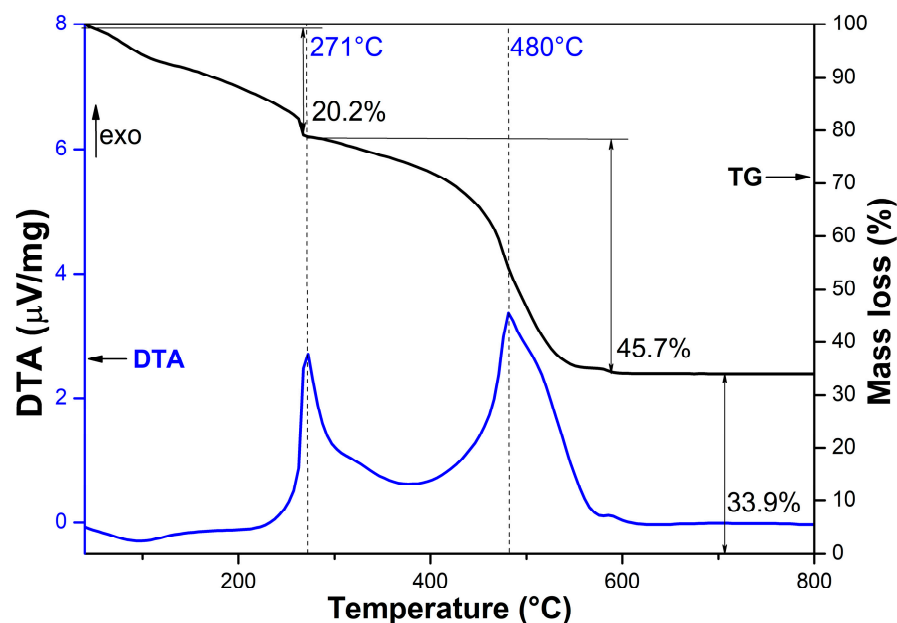


Figure 1. TG-DSC curves of the precursor fibers in air atmosphere.

The shapes of the TG and DTA curves, along with observed events, are in good agreement with the literature sources [32,34,36,38].

Phase analysis—X-ray diffraction. XRD pattern of the Nb₂O₅ NFs obtained from the precursor PAN/Nb₂O₅ composite fibers by calcination at 600 °C is shown in Figure 2a. It exhibits the characteristic diffraction peaks corresponding to the orthorhombic T-phase Nb₂O₅ (T-Nb₂O₅, JCPDS No. 00-030-0873) [21,39]. It is in good agreement with the literature sources where a similar pattern was observed for the samples heat treated below 800 °C [18,21,23,40].

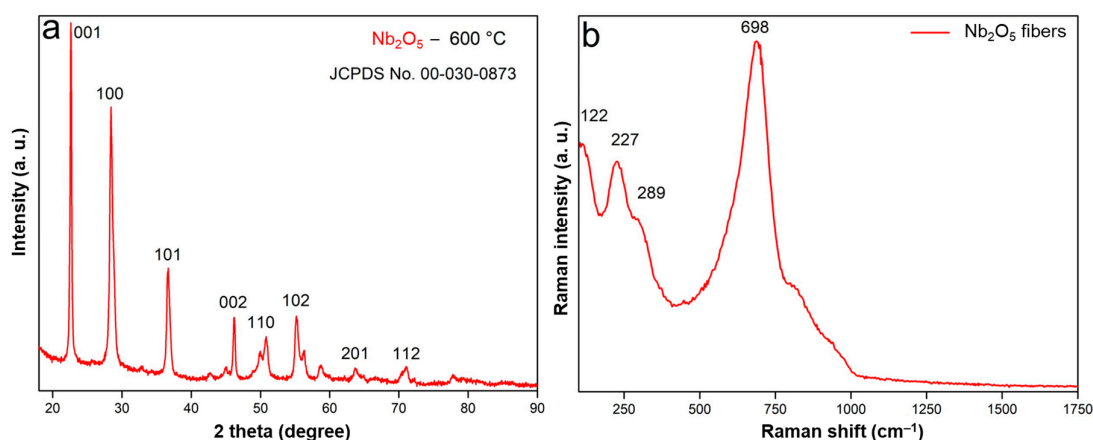


Figure 2. (a) XRD pattern and (b) Raman spectrum of ceramic Nb₂O₅ fibers obtained at 600 °C.

Raman microscopy. The Raman spectrum of Nb₂O₅ calcined at 600 °C is shown in Figure 2b. The peaks characteristic for the T-Nb₂O₅ centered at 122, 227, 300, and 689 cm⁻¹ are in good agreement with the published reference literature [15]. The peaks at

180–350 and 580–740 cm^{-1} are attributed to the Nb–O–Nb angle deformation and bridging bond of distorted NbO_6 clusters [41]. The recorded pattern confirms the results of the XRD measurements.

Electron microscopy. Morphologies of the fibrous samples were studied by SEM in combination with EDX analysis. Results of the morphological studies of the precursor and ceramic fibers, obtained by calcination at 600 °C, are depicted in Figure 3. As can be seen from the micrographs in Figure 3a,b, the electrospun fibers are formed by continuous randomly aligned fibers with a mean diameter of 877 ± 320 nm. The formation mechanism is similar to the one described in the authors' previous works focused on the electrospun TiO_2 fibers [42]. Similarly to the mentioned works, the ceramic precursor reacts with the air moisture, forming the pre-ceramic/polymer composite fibers. However, the slightly lower reactivity of the NbCl_5 (compared to the titanium tetraisopropoxide [42]) results in the prolonged reaction, and thus the formation of the porous internal skeleton of the fibers, instead of the tubular structures, typical for the TiO_2 precursors. Formation of the skeleton and increased porosity are also assisted by the non-solvent-induced phase separation of PAN and hydrolysis products of the NbCl_5 . Calcined fibers are depicted in Figure 3c,d. Although thin ceramic fibers possess some flexibility, high porosity brings brittleness into the system, which is visible in Figure 3. The obtained ceramic fibers have a mean diameter of 614 ± 100 nm. The surface of the ceramic Nb_2O_5 NFs is rough due to the polycrystalline nature and high porosity.

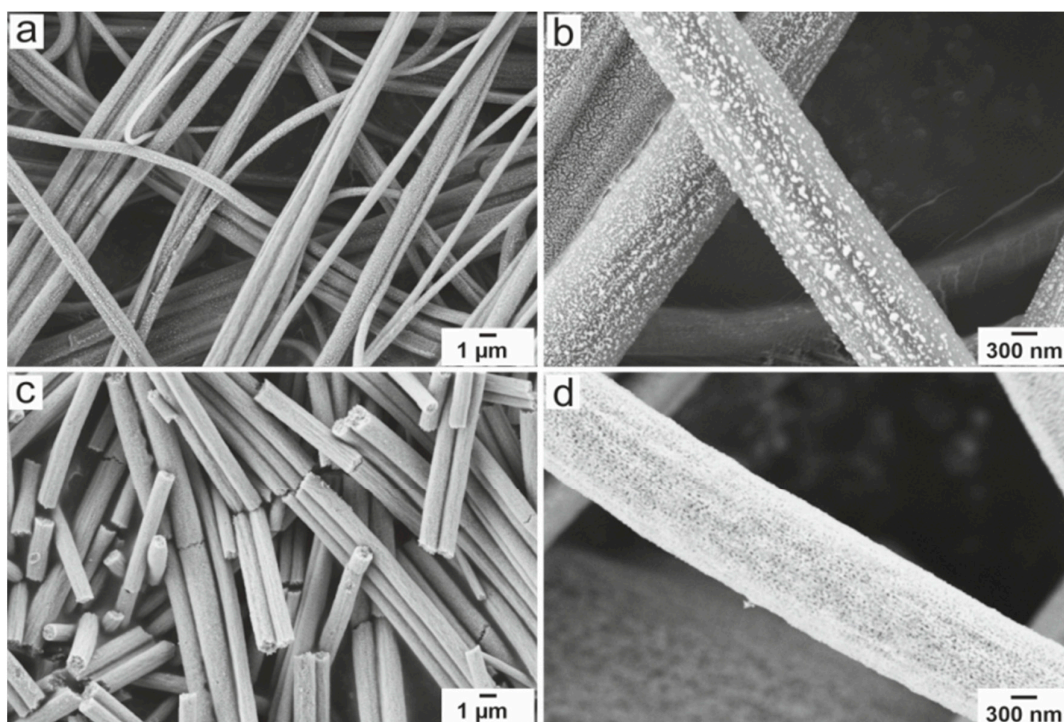


Figure 3. SEM images of (a,b) precursor PAN/ NbCl_5 fibers and (c,d) final ceramic Nb_2O_5 NFs.

For a more detailed study of the prepared ceramic fibers, TEM analysis was performed. The corresponding selected-area electron diffraction (SAED) pattern confirms the polycrystalline character of the sample and corresponds with the results of XRD and Raman microscopy. As depicted in Figure 4a,c, single fibers are made up of grains of 10 to 40 nm in size. EDX maps in Figure 4c showed that distributions of Nb and O were uniform, and the atomic analysis results in 17.92 at.% of Nb and 82.08 at.% of O.

Nitrogen absorption surface area analysis by BET isotherms. Figure 5 depicts the results of the BET analysis of the ceramic Nb_2O_5 NFs calcined at 600 °C. The value of the total surface area was obtained as only 12.8 m^2/g . However, the plot analysis reveals some anomalies; the specific shape of the isotherms presented in Figure 5 confirms the presence

of micropores; this is why the directly obtained S_{BET} value is not fully reliable for this type of sample. To analyze the pores' nature, size distribution, and real surface area, the t-plot method was used. While the results of the surface area analyses are gathered in Table 1, Figure 6 shows the pore size distribution obtained for Nb_2O_5 NFs. As can be seen from the graph, the material is characterized by the dominating large meso- and macropores and the mean pore size is about 22.5 nm. From the point of view of gas absorption, such material has a low surface area. However, for the application of battery electrodes and absorption of liquid electrolytes, these kinds of fibers should provide good fluid mobility and open volume for sulfur immobilization.

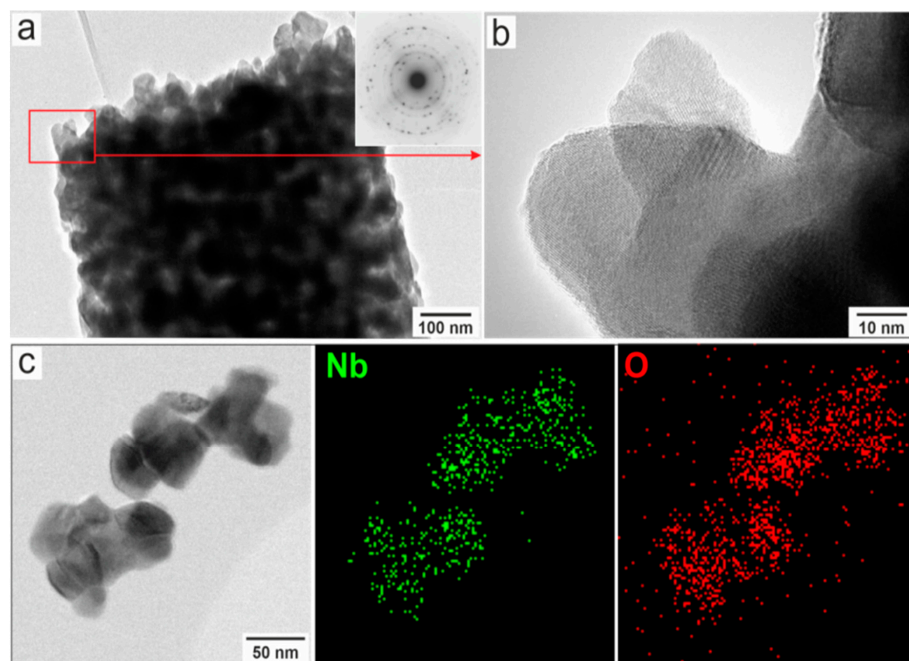


Figure 4. (a) TEM micrograph of Nb_2O_5 fibers with electron beam diffractogram as an inset and (b) HRTEM image (detail) of the fiber from the selected area; (c) TEM/EDX elemental mapping of the fiber grains.

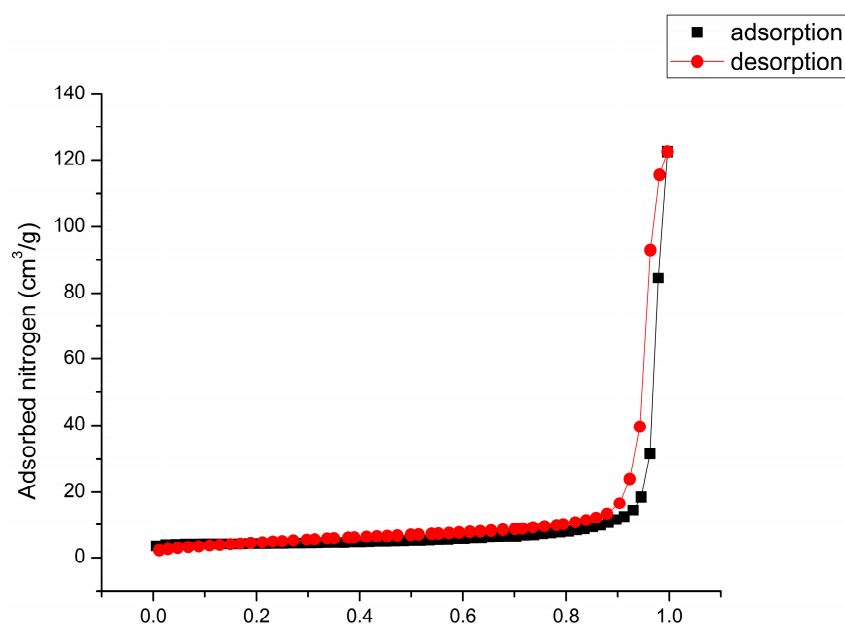
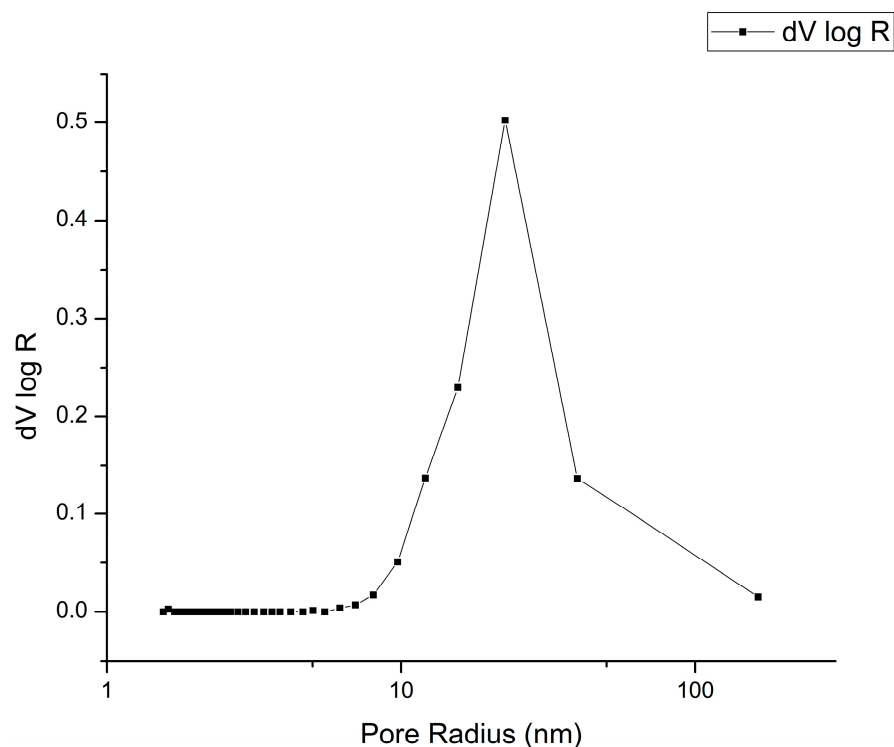


Figure 5. Nitrogen adsorption–desorption isotherms recorded for ceramic Nb_2O_5 NFs.

Table 1. Results of the BET isotherm analysis of Nb₂O₅ NFs.

Sample	S _{BET} , m ² /g	t-Plot Analysis			Mean Pore Size, nm
		V _{micro} , m ³ /g	S _{micro} , m ² /g	S _{ext} , m ² /g	
Nb ₂ O ₅ @600 °C	12.8	0.003	6.989	7.472	22.5

**Figure 6.** Pore size distribution was measured for the ceramic Nb₂O₅ NFs.

2.2. Electrochemical Characterization

Figure 7 depicts SEM micrographs with point EDX analyses of the as-prepared “fresh” electrodes with the addition of Nb₂O₅ NFs and after the electrochemical testing of the last. As can be seen, Nb₂O₅ NFs are perfectly preserved after the electrode preparation and deposition on the aluminum foil collector. Also, there are no visible changes in the morphology of Nb₂O₅ NFs after the electrochemical cycling of the electrode. The only difference visible is the lower content of sulfur, which can be described by the discharged state of the tested and disassembled battery.

The electrochemical properties of the S/Nb₂O₅ cathode in Li-S batteries were evaluated in detail. The cyclic voltammogram (CV) curves at a scan rate of 0.1 mV s^{−1} (see Figure 8a) and exhibits two reduction peaks at 2.3 V and 2.0 V. The first reduction corresponds to the reaction of elemental sulfur with lithium, resulting in higher polysulfides (Li₂S_x, x = 4 – 8), and the second peak may be described by a further reduction to lower polysulfides (Li₂S₃, Li₂S₂) and discharge product (Li₂S), respectively [43]. In the subsequent anodic scan, one can see two oxidation peaks, and the reverse reactions proceed. The current density decreases in the first three scans, although the third and fourth cycles are well overlapped, indicating good stability of the system. The charge capacitances obtained from the integrated area of the current-time representation of the cyclic voltammetry for the anodic and cathodic reactions are almost the same, which means the electrochemical reaction is reversible.

To explore the rate performance of the S/Nb₂O₅ electrode, Li-S battery cells were galvanostatically charged and discharged at different current densities of 0.2 C, 0.5 C, 1 C, and 2 C (see Figure 8b). The discharge capacity in the first cycle at each C-rate was 574, 525,

477, and 368 $\text{mAh}\cdot\text{g}^{-1}$, respectively. The discharge capacity of 680 $\text{mAh}\cdot\text{g}^{-1}$ is acquired when the C-rate is shifted back to 0.2 C. The Coulombic efficiency, despite multi-current cycling, reached the value of 91.6%. The change of charge/discharge profiles at different current densities is demonstrated in Figure 8c. Both plateaus are visible at all C-rates, corresponding to peaks observed in CV. However, plateaus are suppressed for high current density due to limited charge transferability. Charge/discharge curves, despite cycling at 0.2 C, are depicted in Figure 8d. One can see that the plateaus are suppressed in the first cycle, and capacity increases with the number of cycles, demonstrating the reduced impact of the polysulfide shuttle. Here, the high reversibility of the electrochemical reaction is assumed to be provided by the combination of factors. First, the specific porosity of the added Nb_2O_5 fibers, surface area, and chemisorption of the discharge products originated from the chemical nature of the additive.

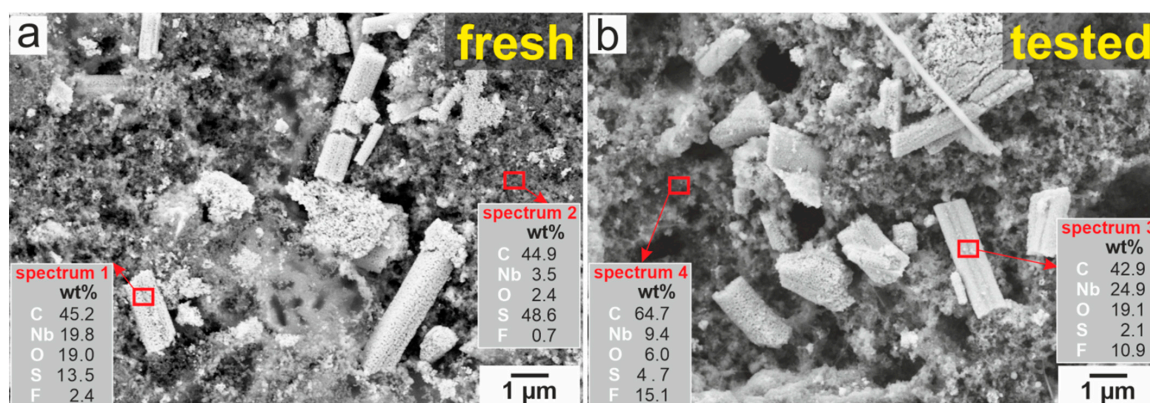


Figure 7. SEM micrographs of the prepared electrodes, depicting Nb_2O_5 fibers embedded in the battery electrode: (a) before the electrochemical tests (marked as “fresh”) with EDX analysis results in the insets; and (b) after the performed electrochemical tests—5 cycles of charging/discharging (marked as “tested”) with EDX analysis results in the insets.

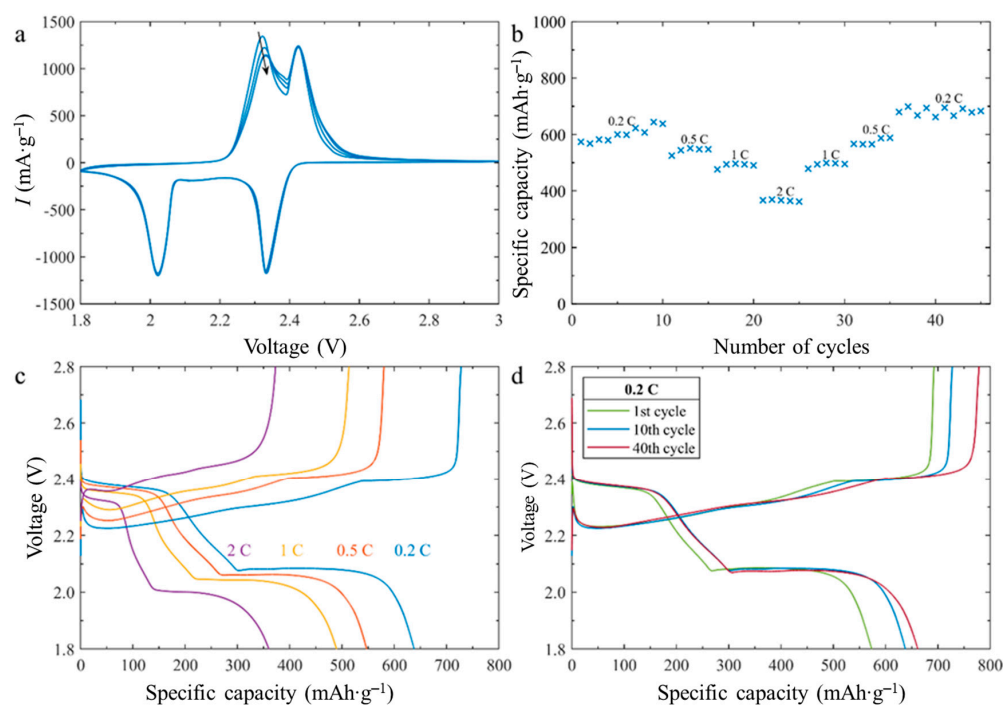


Figure 8. (a) CV profiles the $\text{S}/\text{Nb}_2\text{O}_5$ cathode at a scan rate of 0.1 mV s^{-1} , (b) cycling performance at different C-rate values, (c) charge/discharge profiles despite multi-current cycling, and (d) charge/discharge curves during cycling at 0.2 C.

To further demonstrate the positive effect of the Nb_2O_5 fibers, the cycling stability of the Li-S battery with the $\text{S}/\text{Nb}_2\text{O}_5$ cathode was evaluated during long-term cycling at 0.5 C (see Figure 9a). Capacity increases up to the 50th cycle, then decreases slightly up to the 130th cycle, and with increasing battery degradation, the capacity decrease is more significant. The initial discharge capacity of 0.5 C reached the value of $571 \text{ mAh}\cdot\text{g}^{-1}$. A reversible capacity of $407 \text{ mAh}\cdot\text{g}^{-1}$ is retained after 200 cycles. The capacity retention was 71.3%, representing the capacity fading rate per cycle of 0.144%. The average value of Coulombic efficiency, despite long-term cycling at 0.5 C, was 90.0% and declined during cycling due to the increased influence of the polysulfide shuttle. The galvanostatic charge/discharge profiles during cycling at 0.5 C showed two plateaus corresponding to CV curves. The voltage of the high and low voltage plateau decreases with the degradation of the battery. The obtained results are comparable with results published by the authors for the application of MOFs in LSBs [7].

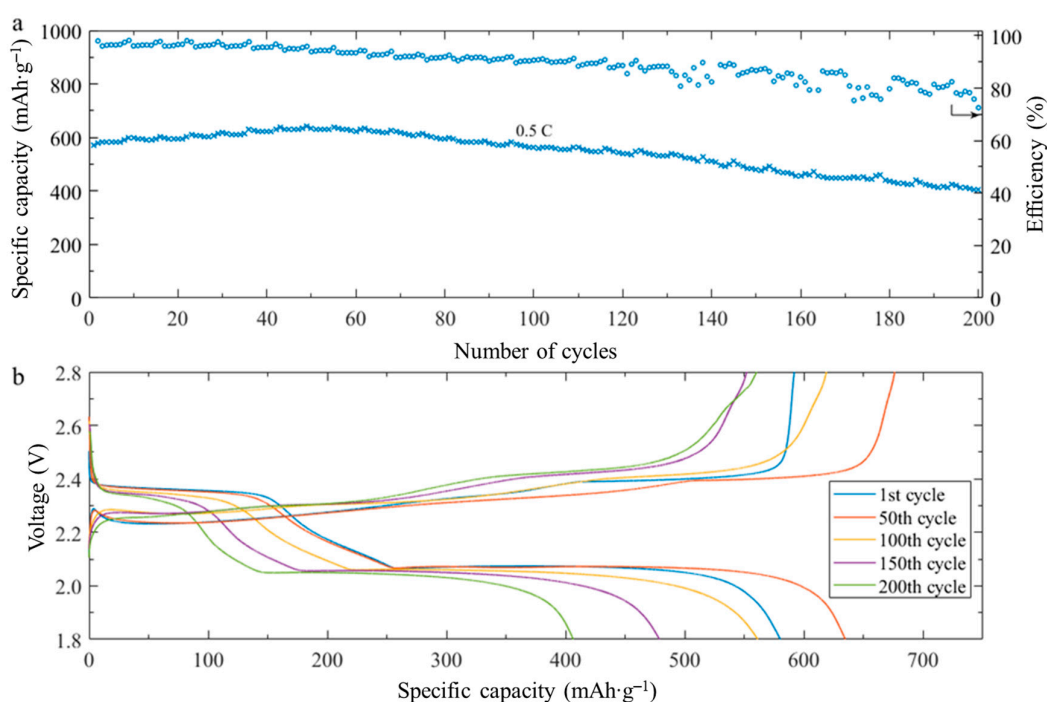


Figure 9. (a) Galvanostatic cycling of the $\text{S}/\text{Nb}_2\text{O}_5$ electrode at 0.5 C for 200 cycles, (b) selected charge/discharge profiles during cycling at 0.5 C.

For the sake of comparison and emphasizing the effect of Nb_2O_5 nanofibers in addition to the cathode material, the same cathode was prepared without ceramic additives and tested similarly. The results of the electrochemical tests are generalized in Figure 10 below.

As can be seen from Figure 10, pure electrodes without ceramic nanofibers addition show lower performance and stability. Figure 10a shows cyclic voltammogram CV curves at a scan rate of 0.1 mV s^{-1} , which exhibit two reduction peaks at 2.3 V and 2.0 V. Similarly, the first reduction corresponds to the interaction of sulfur with lithium, resulting in higher polysulfides. In comparison, the second peak may be ascribed to the further reduction of lower polysulfides and Li_2S discharge product. In the subsequent anodic scan, one can see two oxidation peaks, and the reverse reactions proceed. However, the reversibility of the electrochemical reaction is much lower compared to the first case. The long-term cyclization pointed out that, in the case of the pure carbon electrode, the capacity retention after 200 cycles is only 35%, which is in good agreement with the literature regarding similar composition [44].

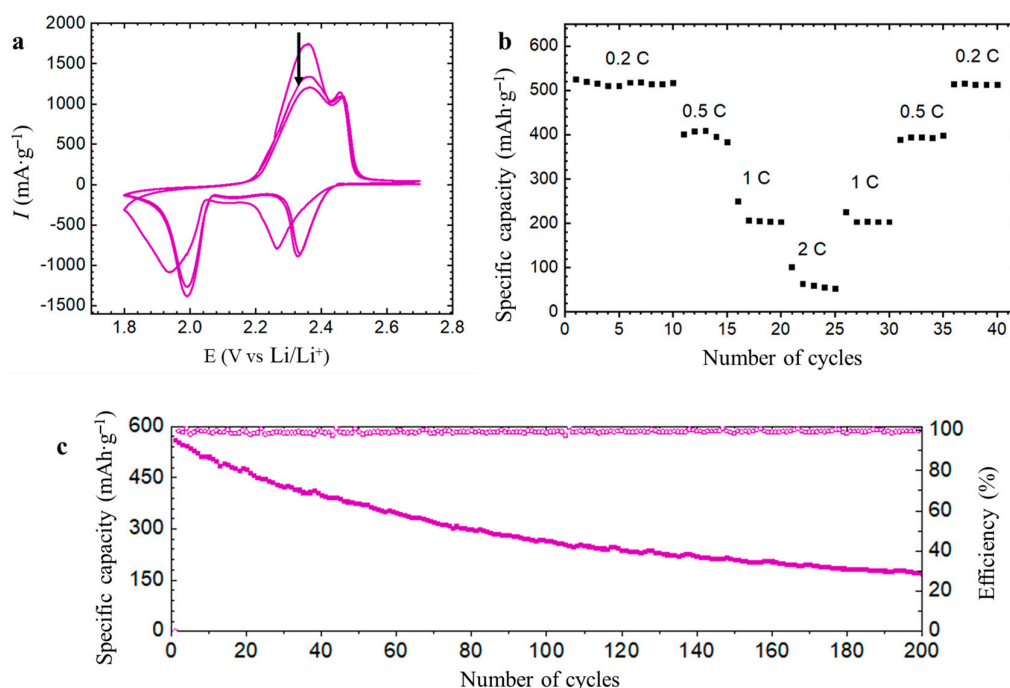


Figure 10. (a) CV profiles the S/C pure cathode at a scan rate of 0.1 mV s^{-1} , (b) cycling performance at different C-rate values, and (c) galvanostatic cycling of the S/C pure cathode at 0.5 C for 200 cycles.

3. Materials and Methods

The fabrication of the ceramic niobium pentoxide fibers consists of three basic steps: preparation of the electrospinning solution, electrospinning of the composite precursor PAN/Nb₂O₅, and its further calcination in air.

The electrospinning solution for the needle-less design was prepared by separately dissolving polyacrylonitrile (PAN, Mw = 150 kDa, Aldrich, now Merck, Darmstadt, Germany) and niobium pentachloride—NbCl₅ (99.8%, Acros Organics, Geel, Belgium) in N,N-dimethylformamide (DMF, Supelco, Merck, Darmstadt, Germany) till full dissolution and then mixed to obtain a solution with a ratio PAN/NbCl₅/DMF 8/10/82. The as-prepared blend was electrospun by reactive needle-less electrospinning technology at IMR SAS Kosice on the Nanospider NSLab200 machine by Elmarco Co (Liberec, Czechia) using the following parameters: wireframe electrode, electrode-to-collector distance $150 \pm 10 \text{ mm}$, 10 rpm of the spinning rate, applied voltage 72 kV, ambient temperature 25 °C, and relative humidity 50%. Here, “reactive” means that simultaneously to the electrospinning process (during the formation and elongation of the fiber, when the surface area rapidly increases), the NbCl₅ reacts with the air moisture, hydrolyses resulting in the formation of the pre-ceramic/polymer composite fibers. For the completion of the hydrolysis process, the as-spun fibers were left overnight in the lab. Removal of the organic component of the precursor fibers was performed by conventional calcination in alumina crucibles in a lab furnace at 600 °C in air and 10 °C/min heating rate.

The thermal decomposition and crystallization of the samples were analyzed by thermogravimetric analysis (TGA, JUPITER STA 449-F1, NETZSCH, Selb, Gebrüder-Netzsch-Straße, Germany) followed by phase composition analysis using X-ray diffraction (XRD, Philips X’PertPro, Amsterdam, Netherlands, with CuK α radiation). Thermogravimetric measurements were performed from room temperature up to 1000 °C under synthetic air flow (50 mL/min) with a heating rate of 10 °C/min using common Al₂O₃ crucibles. TGA measurements with empty Al₂O₃ crucibles were performed to obtain the baselines.

For the detailed chemical composition and phase analysis, a Raman study of the tested fibrous specimens was carried out using a Raman microscope XploRA ONE by HORIBA

Jobin Yvon (Palaiseau, France). A laser with a wavelength of $\lambda = 532$ nm was used, and a spectrum in the range of 100 to 3000 cm^{-1} was recorded.

Morphologies and substructure of the prepared fibrous samples were observed by scanning electron microscopy (SEM/FIB, ZEISS AURIGA Compact, Carl Zeiss, Oberkochen, Germany) and transmission electron microscopy (TEM, JEOL 2100F, Akishima, Tokyo, Japan) both coupled with EDX systems (Oxford Instruments, Abingdon, UK). The image analysis was performed by ImageJ software (v. 1.51j8).

To obtain the value of the specific surface area SBET of the studied material, along with the pores' size distribution, the experimental nitrogen gas adsorption data were processed by the Brunauer-Emmett-Teller (BET) isotherms by Quantachrome NOVA 1200 apparatus (Quantachrome Instruments, Boynton Beach, FL, USA).

Electrochemical characterization of the obtained Nb_2O_5 polycrystalline fibers was performed based on their suitability to be used in LSB. Sulfur (Merck, Darmstadt, Germany), carbon Super P (Timcal, Imerys, Paris, France), and electrospun polycrystalline Nb_2O_5 fibers were ground in a mortar with a pestle to prepare the cathode material. The electrode slurry was prepared by dissolution of polyvinylidene fluoride (PVDF, Aldrich, Merck, Darmstadt, Germany) in *N*-methyl-2-pyrrolidone (NMP, Merck, Darmstadt, Germany) and the mixture of the electrode material was added. The resulting mass ratio of sulfur, carbon Super P, Nb_2O_5 fibers, and PVDF was 60/15/15/10. To prepare electrodes, the homogenous slurry mixed for 24 h was coated on Al foil with carbon surface modification and dried in the oven at 60 °C for 24 h, then uniformly dispersed on the carbon-coated aluminum current collector using a coating bar with 200 μm thickness of the wet film. The weight of sulfur per area was controlled at about 2.7 $\text{mg}\cdot\text{cm}^{-2}$. The electrodes with a diameter of 18 mm were pressed with a pressure of 315 $\text{kg}\cdot\text{cm}^{-2}$. The EL-Cells[®] (EL-Cell, Hamburg, Germany) were assembled with S/ Nb_2O_5 as a working electrode, lithium metal foil as both counter and reference electrode, and a glass fibers separator. The electrolyte was 0.7 M bis-(trifluoromethane) sulfonimide lithium salt (Li-TFSI, Merck, Darmstadt, Germany) dissolved in 1,2-dimethoxyethane (DME, Merck, Darmstadt, Germany) and 1,3-dioxolane (DOL, Merck, Darmstadt, Germany) (2:1 volume ratio) with 0.25 M LiNO_3 (Merck, Darmstadt, Germany) as an additive. The assembly of the electrochemical test cells was carried out in a Jacomex (Dagneux, France) glove box. The electrochemical properties of the prepared electrode material were investigated by both cycling voltammetry (CV) and galvanostatic cycling measurements using Autolab Multi M204 (Metrohm Autolab BV, Utrecht, Netherlands). The CV was measured in the potential window 1.8 – 3.0 V vs. Li/Li^+ with a scan rate of 0.1 mV s^{-1} . Galvanostatic cycling was carried out within the voltage range between 1.8 V and 2.8 V vs. Li/Li^+ .

4. Conclusions

In this work, we reported the detailed preparation and characterization of crystalline ceramic flexible 3D structures based on Nb_2O_5 nanofibers obtained by the reactive needleless electrospinning combined with calcination. The post-spinning treatment conditions applied on the prepared fibrous mats were calcination in air at 600 °C at a heating rate of 10 °C per minute. As a result, ceramic nanofibers with a macroporosity were prepared. The electrochemical properties of the prepared fibrous materials were studied based on their suitability for application in LSBs. Li-S battery cells were galvanostatically charged and discharged at different current densities of 0.2 C, 0.5 C, 1 C, and 2 C, respectively. The discharge capacity in the first cycle at each C-rate was 574 , 525 , 477 , and 368 $\text{mAh}\cdot\text{g}^{-1}$, respectively. The discharge capacity of 679.5 $\text{mAh}\cdot\text{g}^{-1}$ is acquired when the C-rate is shifted back to 0.2 C. Long-term charge–discharge experiments based on the LSBs with Nb_2O_5 nanofibers as electrode material was performed; this allowed us to study the degradation rate of such a battery. The initial discharge capacity of 0.5 C reached the value of 571 $\text{mAh}\cdot\text{g}^{-1}$. A reversible capacity of 407 $\text{mAh}\cdot\text{g}^{-1}$ is retained after 200 cycles. The capacity retention was 71.3% , representing the capacity fading rate per cycle of 0.144% .

Author Contributions: Conceptualization, I.S. and E.M.; investigation, I.S., E.M., A.K., D.C., O.P., F.K., O.M., V.A., M.B., M.L., D.M.-B., D.Z. and J.D.; resources, I.S., E.M. and J.D.; writing—original draft preparation, I.S., E.M. and D.C.; writing—review and editing, I.S., E.M., D.C. and D.Z.; visualization, E.M. and A.K.; supervision, J.D.; project administration, I.S., E.M. and J.D.; funding acquisition, I.S., E.M. and J.D. All authors have read and agreed to the published version of the manuscript.

Funding: This research was funded by the Ministry of Defence of the Slovak Republic under the project No. SEMOD-EL76/49-11/2023, by Operational Programme Integrated Infrastructure, co-financed by the European Regional Development Fund by the project: Advancement and support of R&D for “Centre for diagnostics and quality testing of materials” in the domains of the RIS3 SK specialization, Acronym: CEDITEK II., ITMS2014+ code 313011W442, and by the Operational Program Research and Development, co-financed by the European Regional Development Fund by the project „Research Centre of Advanced Materials and Technologies for Recent and Future Applications “PROMATECH” ITMS: 26220220186.

Data Availability Statement: Data are contained within the article.

Conflicts of Interest: The authors declare no conflict of interest.

References

1. Wen, X.; Xiang, K.; Zhu, Y.; Xiao, L.; Liao, H.; Chen, X.; Chen, H. Nb₂O₅-Decorated Nitrogen-Doped Carbon Nanotube Microspheres for Highly Efficient Sulfur Confinement in Lithium-Sulfur Batteries. *Ind. Eng. Chem. Res.* **2019**, *58*, 8724–8733. [[CrossRef](#)]
2. Manthiram, A.; Fu, Y.; Chung, S.H.; Zu, C.; Su, Y.S. Rechargeable Lithium-Sulfur Batteries. *Chem. Rev.* **2014**, *114*, 11751–11787. [[CrossRef](#)] [[PubMed](#)]
3. Chen, Y.; Kang, Y.; Zhao, Y.; Wang, L.; Liu, J.; Li, Y.; Liang, Z.; He, X.; Li, X.; Tavajohi, N.; et al. A Review of Lithium-Ion Battery Safety Concerns: The Issues, Strategies, and Testing Standards. *J. Energy Chem.* **2021**, *59*, 83–99. [[CrossRef](#)]
4. Kim, T.; Song, W.; Son, D.Y.; Ono, L.K.; Qi, Y. Lithium-Ion Batteries: Outlook on Present, Future, and Hybridized Technologies. *J. Mater. Chem. A* **2019**, *7*, 2942–2964. [[CrossRef](#)]
5. Tian, Y.; Zeng, G.; Rutt, A.; Shi, T.; Kim, H.; Wang, J.; Koettgen, J.; Sun, Y.; Ouyang, B.; Chen, T.; et al. Promises and Challenges of Next-Generation “beyond Li-Ion” Batteries for Electric Vehicles and Grid Decarbonization. *Chem. Rev.* **2021**, *121*, 1623–1669. [[CrossRef](#)] [[PubMed](#)]
6. Tao, X.; Wang, J.; Ying, Z.; Cai, Q.; Zheng, G.; Gan, Y.; Huang, H.; Xia, Y.; Liang, C.; Zhang, W.; et al. Strong Sulfur Binding with Conducting Magnéli-Phase TinO_{2n-1} Nanomaterials for Improving Lithium-Sulfur Batteries. *Nano Lett.* **2014**, *14*, 5288–5294. [[CrossRef](#)] [[PubMed](#)]
7. Capkova, D.; Almasi, M.; Macko, J.; Kiraly, N.; Cech, O.; Cudek, P.; Strakova Fedorkova, A.; Knap, V.; Kazda, T. Activated and Carbonized Metal-Organic Frameworks for Improved Cycle Performance of Cathode Material in Lithium-Sulphur Batteries. *J. Phys. Conf. Ser.* **2022**, *2382*, 012010. [[CrossRef](#)]
8. Choudhury, S. Hybrid Cathode Materials for Lithium-Sulfur Batteries. *Curr. Opin. Electrochem.* **2020**, *21*, 303–310. [[CrossRef](#)]
9. Dong, C.; Gao, W.; Jin, B.; Jiang, Q. Advances in Cathode Materials for High-Performance Lithium-Sulfur Batteries. *iScience* **2018**, *6*, 151–198. [[CrossRef](#)]
10. Wang, X.; Gao, T.; Fan, X.; Han, F.; Wu, Y.; Zhang, Z.; Li, J.; Wang, C. Tailoring Surface Acidity of Metal Oxide for Better Polysulfide Entrapment in Li-S Batteries. *Adv. Funct. Mater.* **2016**, *26*, 7164–7169. [[CrossRef](#)]
11. Fan, X.; Sun, W.; Meng, F.; Xing, A.; Liu, J. Advanced Chemical Strategies for Lithium-Sulfur Batteries: A Review. *Green Energy Environ.* **2018**, *3*, 2–19. [[CrossRef](#)]
12. Liu, Y.; Jiang, S.P.; Shao, Z. Intercalation Pseudocapacitance in Electrochemical Energy Storage: Recent Advances in Fundamental Understanding and Materials Development. *Mater. Today Adv.* **2020**, *7*, 100072. [[CrossRef](#)]
13. Ücker, C.L.; Goetzke, V.; Almeida, S.R.; Moreira, E.C.; Ferrer, M.M.; Jardim, P.L.G.; Moreira, M.L.; Raubach, C.W.; Cava, S. Photocatalytic Degradation of Rhodamine B Using Nb₂O₅ Synthesized with Different Niobium Precursors: Factorial Design of Experiments. *Ceram. Int.* **2021**, *47*, 20570–20578. [[CrossRef](#)]
14. Nunes, B.N.; Lopes, O.F.; Patrocínio, A.O.T.; Bahnemann, D.W. Recent Advances in Niobium-Based Materials for Photocatalytic Solar Fuel Production. *Catalysts* **2020**, *10*, 126. [[CrossRef](#)]
15. Qu, X.; Liu, Y.; Li, B.; Xing, B.; Huang, G.; Zhao, H.; Jiang, Z.; Zhang, C.; Hong, S.W.; Cao, Y. Nanostructured T-Nb₂O₅-Based Composite with Reduced Graphene Oxide for Improved Performance Lithium-Ion Battery Anode. *J. Mater. Sci.* **2020**, *55*, 13062–13074. [[CrossRef](#)]
16. Yuan, J.; Li, X.X.; Liu, J.; Zuo, S.; Li, X.X.; Li, F.; Gan, Y.; He, H.; Xu, X.; Zhang, X.; et al. Pomegranate-like Structured Nb₂O₅/Carbon@N-Doped Carbon Composites as Ultrastable Anode for Advanced Sodium/Potassium-Ion Batteries. *J. Colloid Interface Sci.* **2022**, *613*, 84–93. [[CrossRef](#)] [[PubMed](#)]

17. Barnes, P.; Zuo, Y.; Dixon, K.; Hou, D.; Lee, S.; Ma, Z.; Connell, J.G.; Zhou, H.; Deng, C.; Smith, K.; et al. Electrochemically Induced Amorphous-to-Rock-Salt Phase Transformation in Niobium Oxide Electrode for Li-Ion Batteries. *Nat. Mater.* **2022**, *21*, 795–803. [[CrossRef](#)]
18. Ramakrishna, S.; Le Viet, A.; Reddy, M.V.; Jose, R.; Chowdari, B.V.R. Nanostructured Nb₂O₅ Polymorphs by Electrospinning for Rechargeable Lithium Batteries. *J. Phys. Chem. C* **2010**, *114*, 664–671. [[CrossRef](#)]
19. Deka, S. Nanostructured Mixed Transition Metal Oxide Spinel for Supercapacitor Applications. *Dalton Trans.* **2022**, *52*, 839–856. [[CrossRef](#)]
20. Xiong, L.; Fu, Y.; Luo, Y.; Wei, Y.; Zhang, Z.; Wu, C.; Luo, S.; Wang, G.; Sawtell, D.; Xie, K.; et al. Prospective Applications of Transition Metal-Based Nanomaterials. *J. Mater. Res.* **2022**, *37*, 2109–2123. [[CrossRef](#)]
21. Luo, D.; Zhang, Z.; Li, G.; Cheng, S.; Li, S.; Li, J.; Gao, R.; Li, M.; Sy, S.; Deng, Y.P.; et al. Revealing the Rapid Electrocatalytic Behavior of Ultrafine Amorphous Defective Nb₂O_{5-x} Nanocluster toward Superior Li-S Performance. *ACS Nano* **2020**, *14*, 4849–4860. [[CrossRef](#)] [[PubMed](#)]
22. Pang, Q.; Kundu, D.; Cuisinier, M.; Nazar, L.F. Surface-Enhanced Redox Chemistry of Polysulphides on a Metallic and Polar Host for Lithium-Sulphur Batteries. *Nat. Commun.* **2014**, *5*, 3–10. [[CrossRef](#)] [[PubMed](#)]
23. Nowak, I.; Ziolk, M. Niobium Compounds: Preparation, Characterization, and Application in Heterogeneous Catalysis. *Chem. Rev.* **1999**, *99*, 3603–3624. [[CrossRef](#)] [[PubMed](#)]
24. Rani, R.A.; Zoofakar, A.S.; O'Mullane, A.P.; Austin, M.W.; Kalantar-Zadeh, K. Thin Films and Nanostructures of Niobium Pentoxide: Fundamental Properties, Synthesis Methods and Applications. *J. Mater. Chem. A* **2014**, *2*, 15683–15703. [[CrossRef](#)]
25. Hu, Z.; He, Q.; Liu, Z.; Liu, X.; Qin, M.; Wen, B.; Shi, W.; Zhao, Y.; Li, Q.; Mai, L. Facile Formation of Tetragonal-Nb₂O₅ Microspheres for High-Rate and Stable Lithium Storage with High Areal Capacity. *Sci. Bull.* **2020**, *65*, 1154–1162. [[CrossRef](#)] [[PubMed](#)]
26. Ding, H.; Song, Z.; Zhang, H.; Li, X. Niobium-Based Oxide Anodes toward Fast and Safe Energy Storage: A Review. *Mater. Today Nano* **2020**, *11*, 100082. [[CrossRef](#)]
27. Yang, G.; Zhao, X.; Liao, F.; Cheng, Q.; Mao, L.; Fa, H.; Chen, L. Recent Progress and Applications of Niobium-Based Nanomaterials and Their Composites for Supercapacitors and Hybrid Ion Capacitors. *Sustain. Energy Fuels* **2021**, *5*, 3039–3083. [[CrossRef](#)]
28. Shan, Y.; Zheng, Z.; Liu, J.; Yang, Y.; Li, Z.; Huang, Z.; Jiang, D. Niobium Pentoxide: A Promising Surface-Enhanced Raman Scattering Active Semiconductor Substrate. *npj Comput. Mater.* **2017**, *3*, 11. [[CrossRef](#)]
29. Prado, A.C.F.; Malafatti, J.O.D.; Oliveira, J.A.; Ribeiro, C.; Joya, M.R.; Luz, A.P.; Paris, E.C. Preparation and Application of Nb₂O₅ Nanofibers in CO₂ Photoconversion. *Nanomaterials* **2021**, *11*, 3268. [[CrossRef](#)]
30. Silva, M.K.; Marques, R.G.; Machado, N.R.C.F.; Santos, O.A.A. Evaluation of Nb₂O₅ and Ag/Nb₂O₅ in the Photocatalytic Degradation of Dyes from Textile Industries. *Braz. J. Chem. Eng.* **2002**, *19*, 359–363. [[CrossRef](#)]
31. Cheong, J.Y.; Youn, D.Y.; Kim, C.; Jung, J.W.; Ogata, A.F.; Bae, J.G.; Kim, I.D. Ag-Coated One-Dimensional Orthorhombic Nb₂O₅ Fibers as High Performance Electrodes for Lithium Storage. *Electrochim. Acta* **2018**, *269*, 388–396. [[CrossRef](#)]
32. Xue, T.J.; McKinney, M.A.; Wilkie, C.A. The Thermal Degradation of Polyacrylonitrile. *Polym. Degrad. Stab.* **1997**, *58*, 193–202. [[CrossRef](#)]
33. Storck, J.L.; Grothe, T.; Tuvshinbayar, K.; Diestelhorst, E.; Wehlage, D.; Brockhagen, B.; Wortmann, M.; Frese, N.; Ehrmann, A. Stabilization and Incipient Carbonization of Electrospun Polyacrylonitrile Nanofibers Fixated on Aluminum Substrates. *Fibers* **2020**, *8*, 55. [[CrossRef](#)]
34. Samimi-Sohrforozani, E.; Azimi, S.; Abolhasani, A.; Malekian, S.; Arbab, S.; Zendehtdel, M.; Abolhasani, M.M.; Yaghoobi Nia, N. Development of Porous Polyacrylonitrile Composite Fibers: New Precursor Fibers with High Thermal Stability. *Electron. Mater.* **2021**, *2*, 454–465. [[CrossRef](#)]
35. Zhang, H.; Quan, L.; Gao, A.; Tong, Y.; Shi, F.; Xu, L. Thermal Analysis and Crystal Structure of Poly(Acrylonitrile-Co-Itaconic Acid) Copolymers Synthesized in Water. *Polymers* **2020**, *12*, 221. [[CrossRef](#)]
36. Ren, Y.; Huo, T.; Qin, Y.; Liu, X. Preparation of Flame Retardant Polyacrylonitrile Fabric Based on Sol-Gel and Layer-by-Layer Assembly. *Materials* **2018**, *11*, 483. [[CrossRef](#)] [[PubMed](#)]
37. Mudra, E.; Streckova, M.; Pavlinak, D.; Medvecka, V.; Kovacik, D.; Kovalcikova, A.; Zubko, P.; Girman, V.; Dankova, Z.; Koval, V.; et al. Development of Al₂O₃ electrospun Fibers Prepared by Conventional Sintering Method or Plasma Assisted Surface Calcination. *Appl. Surf. Sci.* **2017**, *415*, 90–98. [[CrossRef](#)]
38. Martin, S.C.; Liggat, J.J.; Snape, C.E. In Situ NMR Investigation into the Thermal Degradation and Stabilisation of PAN. *Polym. Degrad. Stab.* **2001**, *74*, 407–412. [[CrossRef](#)]
39. Liu, J.; Xue, D.; Li, K. Single-Crystalline Nanoporous Nb₂O₅ Nanotubes. *Nanoscale Res. Lett.* **2011**, *6*, 138. [[CrossRef](#)]
40. de MGomes, G.H.; de Andrade, R.R.; Mohallem, N.D.S. Investigation of Phase Transition Employing Strain Mapping in TT- and T-Nb₂O₅ Obtained by HRTEM Micrographs. *Micron* **2021**, *148*, 103112. [[CrossRef](#)]
41. Lim, E.; Jo, C.; Kim, H.; Kim, M.H.; Mun, Y.; Chun, J.; Ye, Y.; Hwang, J.; Ha, K.S.; Roh, K.C.; et al. Facile Synthesis of Nb₂O₅@Carbon Core-Shell Nanocrystals with Controlled Crystalline Structure for High-Power Anodes in Hybrid Supercapacitors. *ACS Nano* **2015**, *9*, 7497–7505. [[CrossRef](#)] [[PubMed](#)]
42. Shepa, I.; Mudra, E.; Vojtko, M.; Milkovic, O.; Dankova, Z.; Antal, V.; Annušová, A.; Majková, E.; Dusza, J. Influence of the Polymer Precursor Blend Composition on the Morphology of the Electrospun Oxide Ceramic Fibers. *Results Phys.* **2019**, *13*, 102243. [[CrossRef](#)]

43. Huang, X.; Wang, Z.; Knibbe, R.; Luo, B.; Ahad, S.A.; Sun, D.; Wang, L. Cyclic Voltammetry in Lithium–Sulfur Batteries—Challenges and Opportunities. *Energy Technol.* **2019**, *7*, 1801001. [[CrossRef](#)]
44. Cheng, M.; Liu, Y.; Guo, X.; Wu, Z.; Chen, Y.; Li, J.; Li, L.; Zhong, B. A Novel Binder-Sulfonated Polystyrene for the Sulfur Cathode of Li-S Batteries. *Ionics* **2017**, *23*, 2251–2258. [[CrossRef](#)]

Disclaimer/Publisher’s Note: The statements, opinions and data contained in all publications are solely those of the individual author(s) and contributor(s) and not of MDPI and/or the editor(s). MDPI and/or the editor(s) disclaim responsibility for any injury to people or property resulting from any ideas, methods, instructions or products referred to in the content.